SIAM J. NUMER. ANAL.
Vol. 49, No. 5, pp. 1991–2016

LOCATING SEVERAL SMALL INCLUSIONS IN IMPEDANCE TOMOGRAPHY FROM BACKSCATTER DATA*

MARTIN HANKE†

Abstract. This paper investigates backscatter data for the inverse obstacle problem in impedance tomography, when the obstacles are small. It is shown that under this circumstance the backscatter data are close approximations of a rational function that has second or fourth order poles at the locations of the obstacles. Furthermore, a numerical method is presented to locate the obstacles via the poles of certain Laurent–Padé approximations. Numerical experiments explore the potential of this algorithm also for extended obstacles, taking into consideration that the problem is severely ill-posed.

Key words. impedance tomography, backscatter data, Laurent–Padé approximation

AMS subject classifications. 35R30, 65N21, 41A21

DOI. 10.1137/100810290

1. Introduction.

The inverse obstacle problem in impedance tomography is concerned with the reconstruction of inclusions within a (bounded) homogeneous object (here, the two-dimensional unit disk) that differ in their electrical properties. To this end, potentials on the surface of the object are measured for various boundary currents as excitations. Mostly, data sets for this purpose are discrete approximations of the (full or local) Neumann–Dirichlet map of the associated elliptic differential operator (cf. Adler, Gaburro, and Lionheart [1]), and for these data there exist versatile reconstruction methods; cf., e.g., [14].

The situation is much more difficult if one or only a few boundary currents can be imposed. In this case it is generally an open problem whether the inclusions are uniquely determined by the given data; still, methods based on rational approximations have been suggested in the literature to locate the inclusions (cf., e.g., [6, 7, 13]), and one may use those results to proceed by Newton-type schemes to determine their exact position and shape; cf. [18].

More recently, in [16], a different set of data has been introduced for the two-dimensional inverse obstacle problem. These data have been called *backscatter data* because of an obvious resemblance to similar problem settings in inverse scattering. Backscatter data differ from usual data sets in impedance tomography in that the boundary excitations are dipole-type currents, and that for each excitation the measurements consist of one single number, namely the induced voltage at the current source. It has been shown in [16] that these data suffice to identify a single insulating obstacle within the object. The theory in [16] can be turned into a reconstruction algorithm for the case that there is only one inclusion present which is insulating; cf. Hollborn [20]. Aside of that, another constructive inversion scheme for backscatter data has been designed in [17] which approximates the convex hull of a collection of inclusions of arbitrary types. Presently, these two are the only available algorithms

*Received by the editors October 1, 2010; accepted for publication (in revised form) July 14, 2011; published electronically October 6, 2011. This work has been supported by the Deutsche Forschungsgemeinschaft (DFG) under grant HA 2121/6.
http://www.siam.org/journals/sinum/49-5/81029.html
†Institut für Mathematik, Johannes Gutenberg-Universität Mainz, 55099 Mainz, Germany (hanke@math.uni-mainz.de).

for the reconstruction of obstacles from given backscatter data, and they both share the disadvantage that they are unable to separate multiple inclusions.

Therefore, the main goal of the present work is to provide means to identify and locate multiple inclusions from backscatter data of impedance tomography. To this end, our starting point is an important observation from [17], namely that backscatter data extend as analytic functions up to the (outer) boundaries of (finitely many) inclusions. Here we further analyze the properties of this analytic function and focus on the case that the obstacles shrink to a finite number of points, much in the spirit of recent work on multiple signal classification (MUSIC)-type algorithms for impedance tomography; cf. Ammari and Kang [3]. It turns out that the dominating term of the analytic expansion of the backscatter data (with respect to the size of the inclusions) is a rational function whose poles are precisely these limit points, as well as their reflections at the unit circle (see Theorem 5.2). Generically, the multiplicity of these poles is four, but may degenerate to two for certain cases, including the important special instance of circular inclusions.

Motivated by this result we employ rational approximation methods to detect the locations of multiple inclusions numerically. More precisely, we use so-called $(m-2,m)$-Laurent–Padé approximations for this purpose because of certain specific properties of the analytic extension of the backscatter data; see Theorem 5.1. Numerical experiments support our claim that the poles of these functions can be used to locate the inclusions, even when they have some finite extent. However, as the problem is severely ill-posed, the quality of the reconstructions depends on the amount of noise in the data, but some particular techniques can be incorporated to stabilize the numerical results.

The outline of this work is as follows. In section 2 we recall the precise definition of backscatter data for impedance tomography. Then, in section 3 we lay the groundwork for the asymptotic analysis in section 4 of the backscatter data for small inclusions. More precisely, we develop a new factorization (Theorem 3.1) of the difference of two Neumann–Dirichlet operators associated with the impedance tomography problem, and this factorization provides comparatively easy access to the asymptotic analysis of the impedance tomography problem for small inclusions (based on potential theory for continuous densities, rather than Sobolev spaces as in [3])—for the prize of somewhat stronger assumptions on the smoothness of the inclusions. For our main result we have to rephrase the forward problem in complex variables; this is done in section 5. Finally, section 6 and an appendix briefly recall the notion of Laurent–Padé approximations and outline our approach for the inverse problem. The details of our algorithm and numerical results for data of different qualities are discussed in section 7.

2. Backscatter data. We denote by B the two-dimensional unit disk (the "object") and by

$$\Omega = \bigcup_{j=1}^{J} \Omega_j \subset B \tag{2.1}$$

the union of J simply connected domains (the "inclusions") with C^2 boundaries $\Gamma_j = \partial\Omega_j$ and $\Gamma = \cup\Gamma_j$; cf. Figure 2.1. We assume that the closures of Ω_j are mutually disjoint and do not touch the unit circle $T = \partial B$. Finally, we denote by ν the outer unit normals of the domains Ω_j and B, respectively.

To keep matters simple we restrict the conductivity σ within the object to being

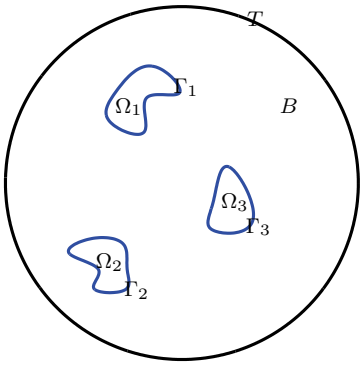

FIG. 2.1. *Geometry and notation.*

piecewise constant, i.e.,

$$\sigma(x) = \begin{cases} \kappa_j\,, & x \in \Omega_j\,, \\ 1 & \text{else}\,, \end{cases} \tag{2.2}$$

where each κ_j is assumed to be positive and different from 1. Then the conductivity equation (to be interpreted in weak form) is given as

$$\nabla \cdot (\sigma \nabla u) = 0 \quad \text{in } B\,, \qquad \frac{\partial}{\partial \nu} u = f \quad \text{on } T\,, \qquad \int_T u \, \mathrm{d}s = 0\,, \tag{2.3}$$

where u is the induced electric potential when a current

$$f \in \mathcal{L}^2_\diamond(T) := \left\{ f \in \mathcal{L}^2(T) \,:\, \int_T f \, \mathrm{d}s = 0 \right\}$$

is imposed on the boundary of the object. Problem (2.3) has a classical interpretation as a diffraction problem with jump conditions

$$u^+ = u^- \qquad \text{and} \qquad \frac{\partial}{\partial \nu} u^+ = \kappa_j \frac{\partial}{\partial \nu} u^- \qquad \text{on } \Gamma_j,\ j = 1, \ldots, J\,; \tag{2.4}$$

cf. Ladyzhenskaya [24]; here we have written u^+ and u^- for the restrictions of u to $B \setminus \overline{\Omega}$ and Ω, respectively. We also need to introduce the reference potential $u_{\mathbb{1}}$ for the case that the object had no inclusions, i.e.,

$$\Delta u_{\mathbb{1}} = 0 \quad \text{in } B\,, \qquad \frac{\partial}{\partial \nu} u_{\mathbb{1}} = f \quad \text{on } T\,, \qquad \int_T u_{\mathbb{1}} \, \mathrm{d}s = 0\,. \tag{2.5}$$

We mention that (2.4) remains valid when we allow some of the inclusions to be insulating, i.e., when we formally set $\kappa_j = 0$ for the respective conductivities. The corresponding potential u is only determined in the exterior of the insulating cavities and has homogeneous Neumann boundary values at their boundaries; however, u can be extended continuously by a harmonic function in the interior of these inclusions, such that the extension satisfies (2.4). With this understanding, all the results that we obtain below extend to insulating inclusions by setting the corresponding parameters to be $\kappa_j = 0$.

Associated with the two boundary value problems (2.3) and (2.5) are the two Neumann–Dirichlet operators Λ and $\Lambda_{\mathbb{1}}$, which map f onto the Dirichlet values of the associated potentials, namely,

$$\Lambda \,:\, \begin{cases} \mathcal{L}^2_\diamond(T) \to \mathcal{L}^2_\diamond(T)\,, \\ \qquad f \mapsto u|_T\,, \end{cases}$$

with u of (2.3), and $\Lambda_{\mathbb{1}}$ being defined accordingly with $u_{\mathbb{1}}$ instead of u. These two operators are known to be bounded and self-adjoint operators, and we will make use of the associated symmetric quadratic form

$$Q[f] \,=\, \langle\, f, (\Lambda - \Lambda_{\mathbb{1}}) f \,\rangle\,. \tag{2.6}$$

The angle brackets in (2.6) refer to the standard bilinear form in $\mathcal{L}^2(T)$; we mention, however, that—in view of our assumptions (2.2) on the conductivity σ—Q has a well-defined extension to any $f \in H^{-s}_\diamond(T)$, where $H^{-s}_\diamond(T)$ is the Sobolev space of negative order $-s < 0$ whose elements are restricted to having a vanishing mean; here, s may be arbitrarily large; cf. [17, Appendix].

Backscatter data for impedance tomography have recently been introduced in [16, 17]. Formally, these are defined as the function b given by

$$b(\theta) \,=\, Q[\delta'_{x_\theta}]\,, \qquad 0 \le \theta < 2\pi\,, \tag{2.7}$$

where δ'_{x_θ} denotes the tangential derivative of the delta distribution located in the boundary point $x_\theta = (\cos\theta, \sin\theta) \in T$, i.e.,

$$\langle\, \delta'_{x_\theta}, g \,\rangle \,=\, -\frac{\partial}{\partial\theta} g(x_\theta)$$

for g sufficiently smooth; in fact, $\delta'_{x_\theta} \in H^{-3/2-\varepsilon}_\diamond(T)$ for any positive number ε. Physically, the backscatter $b(\theta)$ is the first order voltage variation that is induced by the presence of the inclusions Ω if the body is exposed to a fixed amount of current between two thin electrodes in the vicinity of x_θ; see [15] for a rigorous statement of this result.

3. Factorization of $\Lambda - \Lambda_{\mathbb{1}}$. To prepare the groundwork for our analysis we first introduce the Neumann function associated with the Laplacian in the unit disk, i.e.,

$$N(x,z) \,=\, \begin{cases} -\dfrac{1}{2\pi}\left(\log|z-x| \,+\, \log\Big|\dfrac{z}{|z|} - |z|x\Big|\right), & z \ne 0\,, \\ -\dfrac{1}{2\pi}\,\log|x|\,, & z = 0\,. \end{cases} \tag{3.1}$$

Then the reference potential $u_{\mathbb{1}}$ of (2.5) can be represented as a single layer potential

$$u_{\mathbb{1}}(x) \,=\, \int_T N(x,y) f(y)\, \mathrm{d}s(y)\,, \qquad x \in B\,,$$

and its flux across Γ is given by

$$\frac{\partial}{\partial\nu} u_{\mathbb{1}}(x) \,=\, (Af)(x) \,=\, \int_T \frac{\partial}{\partial_x \nu} N(x,y)\, f(y)\, \mathrm{d}s(y)\,, \qquad x \in \Gamma\,; \tag{3.2}$$

bear in mind that ν is pointing into the *exterior* of Ω.

Because of our assumption that Ω is C^2 smooth, the expression (3.2) is a continuous function of $x \in \Gamma$ and, in view of Green's theorem, can be considered an element of

$$C_\diamond(\Gamma) \,=\, \left\{ \varphi \in C(\Gamma) \,:\, \int_{\Gamma_j} \varphi \, \mathrm{d}s \,=\, 0\,,\ j = 1, \ldots, J \right\}.$$

Moreover, A is a bounded operator from $H_\diamond^{-s}(T)$ to $C_\diamond(\Gamma)$, where s may be any positive number; cf. [17, Appendix]. The Banach spaces $C_\diamond(\Gamma)$ and

$$C_*(\Gamma) \,=\, \big(C(\Gamma_1)/\mathbb{R}\big) \,\oplus\, \big(C(\Gamma_2)/\mathbb{R}\big) \,\oplus\, \cdots \,\oplus\, \big(C(\Gamma_J)/\mathbb{R}\big)\,, \tag{3.3}$$

where an equivalence class of functions in $C_*(\Gamma)$ consists of those elements of $C(\Gamma)$ that differ on each component Γ_j of Γ by an individual constant, define a dual system (cf. Kress [22, Definition 4.2]) with respect to the standard L^2 inner product. Likewise, $H_\diamond^{-s}(T)$ and $H_\diamond^s(T)$ also define a dual system. The associated dual (or adjoint) operator of A, denoted by $A^* : C_*(\Gamma) \to H_\diamond^s(T)$, provides the trace on T of an (augmented) double layer potential w, i.e.,

$$w(x) \,=\, (A^*\psi)(x) \,=\, \int_\Gamma \frac{\partial}{\partial_y \nu} N(x,y)\, \psi(y)\, \mathrm{d}s(y)\,, \qquad x \in T\,. \tag{3.4}$$

We remark that a density ψ that is constant on each component Γ_j of Γ belongs to the null space of the formal extension of A^* to all of $C(\Gamma)$, and vice versa; hence in (3.3) we have factored out the null space of A^*.

We will also need the (augmented) double layer operator

$$(K^N\psi)(x) \,=\, \int_\Gamma \frac{\partial}{\partial_y \nu} N(x,y)\, \psi(y)\, \mathrm{d}s(y)\,, \qquad x \in \Gamma\,.$$

Again note that densities that are constant on each Γ_j, $j = 1, \ldots, J$, are eigenfunctions of K^N. Accordingly, K^N is a well-defined compact operator from $C_*(\Gamma)$ to $C_*(\Gamma)$; we refer to [3, 22] for basic properties of this operator. Finally, we introduce the Neumann–Dirichlet operator

$$\lambda : C_\diamond(\Gamma) \to C_*(\Gamma) \tag{3.5}$$

of the Laplacian in Ω. Note that it follows from the material in [3, 22] that this Neumann–Dirichlet map is a bounded operator between these topologies.

Now we can formulate our first result.

THEOREM 3.1. *For the difference $\Lambda - \Lambda_{\mathbb{1}}$ of the two Neumann–Dirichlet operators on B we have the factorization*

$$\Lambda - \Lambda_{\mathbb{1}} \,=\, A^*(E - K^N)^{-1}\lambda A\,, \tag{3.6}$$

where $E : C_*(\Gamma) \to C_*(\Gamma)$ is the "diagonal operator" defined by

$$(E\chi)|_{\Gamma_j} \,=\, \frac{1}{2}\frac{1+\kappa_j}{1-\kappa_j}\, \chi|_{\Gamma_j}\,, \qquad j = 1, \ldots, J\,,$$

for $\chi \in C_*(\Gamma)$.

Proof. Let $f \in \mathcal{L}^2_\diamond(T)$ be a given boundary current, and let $u_{\mathbb{1}}$ be given by (2.5). It then follows from (3.2) that

$$u_{\mathbb{1}}|_\Gamma = \lambda A f \tag{3.7}$$

in the sense of $C_*(\Gamma)$. With u of (2.3) define

$$w = \begin{cases} u^+ - u_{\mathbb{1}} & \text{in } B \setminus \overline{\Omega}\,, \\ \kappa_j u^- - u_{\mathbb{1}} & \text{in } \Omega_j\,,\ j = 1, \ldots, J\,. \end{cases} \tag{3.8}$$

Then w satisfies

$$\Delta w = 0 \quad \text{in } B \setminus \Gamma\,, \qquad \frac{\partial}{\partial \nu} w^+ = \frac{\partial}{\partial \nu} w^- \quad \text{on } \Gamma\,,$$

$$\int_T w \, \mathrm{d}s = 0\,, \qquad \frac{\partial}{\partial \nu} w = 0 \quad \text{on } T\,,$$

and hence coincides with the (augmented) double layer potential over Γ with density

$$\psi = w^+|_\Gamma - w^-|_\Gamma\,,$$

as is obvious from the jump conditions of double layer potentials; cf., e.g., [3].[1] In particular (cf. (3.4)), we have

$$A^* \psi = w|_T = (u - u_{\mathbb{1}})|_T = (\Lambda - \Lambda_{\mathbb{1}}) f\,. \tag{3.9}$$

We can express ψ in terms of the respective traces of $u_{\mathbb{1}}$ and $u^+ = u^-$ on Γ_j, $j = 1, \ldots, J$ (cf. (2.4)) as

$$\psi = u^+ - u_{\mathbb{1}} - (\kappa_j u^- - u_{\mathbb{1}}) = u^+ - \kappa_j u^- = (1 - \kappa_j) u^-\,. \tag{3.10}$$

Using once again the jump relations of the double layer potential, the inner trace of w on Γ is given by

$$w^- = K^N \psi - \frac{1}{2}\,\psi\,,$$

and hence on Γ_j there holds

$$\big((E - K^N)\psi\big)\big|_{\Gamma_j} = \Big(\frac{1}{2}\frac{1 + \kappa_j}{1 - \kappa_j} - \frac{1}{2}\Big)\psi|_{\Gamma_j} - w^-|_{\Gamma_j}\,.$$

Inserting now the definition (3.8) of w and (3.10), it follows that

$$(E - K^N)\psi = \frac{\kappa_j}{1 - \kappa_j}\,\psi - (\kappa_j u^- - u_{\mathbb{1}}) = u_{\mathbb{1}}$$

on Γ_j, for each $j = 1, \ldots, J$, i.e., that

$$(E - K^N)\psi = \lambda A f \tag{3.11}$$

in the sense of $C_*(\Gamma)$; cf. (3.7). Following the line of argument in the proof of [3, Lemma 2.18] it can be seen that $E - K^{N*} : C_\diamond(\Gamma) \to C_\diamond(\Gamma)$ is injective. As both

[1] Note that the authors of [3] employ a fundamental solution of opposite sign.

K^N and K^{N*} are compact, the Riesz–Fredholm theory implies that $E - K^N$ is also injective and does have a bounded inverse (cf., e.g., [22, Theorem 4.15]). Thus the assertion (3.6) follows from (3.9) and (3.11). □

There is a similar factorization of $\Lambda - \Lambda_{\mathbb{1}}$, in which A and A^* are replaced by single layer operators S and S^*, respectively:

$$\Lambda - \Lambda_{\mathbb{1}} \;=\; S^* \big(E^* - K^{N*}\big)^{-1} \lambda^{-1} S\,. \tag{3.12}$$

This factorization (somewhat less specific though, as the assumptions on σ were more general) has been utilized in [17] and also appears in the work of Kress and Kühn [23, Theorem 3.1]. The particular form (3.12) is also implicit in [3, p. 135].

4. Asymptotic behavior of the backscatter data for small inclusions. From now on we assume that the inclusions are given by

$$\Omega_j \;=\; x_j \,+\, \varepsilon O_j, \qquad j = 1, \ldots, J\,, \tag{4.1}$$

where ε is a positive number, x_j, $j = 1, \ldots, J$, are distinct points in B, and each of the simply connected domains O_j contains the origin in its convex hull and has a C^2 boundary; note that ε must be sufficiently small so as to fulfill the requirements on Ω_j from section 2; cf. (2.1). We refer to x_j as the "location" of Ω_j and to O_j as its "shape." Our plan is to investigate the backscatter data $b : [0, 2\pi) \to \mathbb{R}$ as ε goes to zero. Considerations of this sort go back to the seminal paper by Friedman and Vogelius [10] and have since been popularized by the extensive work of Ammari, Kang, and coauthors; cf., e.g., [3, 4] and the references therein. To facilitate the presentation, we refrain from augmenting subscripts ε to all relevant symbols.

We start by investigating the operator $E - K^N$ which appears in the center of the factorization of Theorem 3.1. As in [2, sect. 6] we consider $E - K^N$ as a $J \times J$ matrix of integral operators acting from $C(\Gamma_i)/\mathbb{R}$ to $C(\Gamma_j)/\mathbb{R}$, and whose "diagonal" is the operator $D^N : C_*(\Gamma) \to C_*(\Gamma)$ defined by

$$\big(D^N \varphi\big)\big|_{\Gamma_j} \;=\; \Big(\frac{1}{2} \frac{1+\kappa_j}{1-\kappa_j}\, I - K_j^N \Big) \varphi|_{\Gamma_j}\,, \qquad j = 1, \ldots, J\,, \tag{4.2}$$

where

$$(K_j^N \varphi_j)(x) \;=\; \int_{\Gamma_j} \frac{\partial}{\partial_y \nu} N(x,y)\, \varphi_j(y)\; \mathrm{d}s(y)\,, \qquad x \in \Gamma_j\,,$$

is the (augmented) double layer operator over the boundary Γ_j, and I always denotes the respective identity operator. Recall (cf. (3.1)) that the Neumann function $N(x,y)$ differs from the fundamental solution $\Phi(x,y) = -\frac{1}{2\pi} \log|x-y|$ of the Laplacian by a function that is smooth and bounded for y strictly separated from T; accordingly, the difference between K_j^N and the (standard) double layer operator

$$(K_j \varphi_j)(x) \;=\; \frac{1}{2\pi} \int_{\Gamma_j} \frac{(x-y)\cdot \nu(y)}{|x-y|^2}\, \varphi_j(y)\; \mathrm{d}s(y)\,, \qquad x \in \Gamma_j\,,$$

is an operator from $C_*(\Gamma)$ to $C_*(\Gamma)$ whose operator norm can be bounded by some constant times the length $|\Gamma_j|$ of the boundary. Using also the fact that the "off-diagonal entries" of $E - K^N$ consist of integral operators with smooth kernel functions over the boundaries Γ_j, it follows from (4.2) that

$$E - K^N \;=\; D + R\,, \tag{4.3}$$

where the diagonal operator $D : C_*(\Gamma) \to C_*(\Gamma)$ is given by

$$(D\varphi)\big|_{\Gamma_j} \;=\; \Big(\frac{1}{2}\frac{1+\kappa_j}{1-\kappa_j}\,I - K_j\Big)\varphi|_{\Gamma_j} \;=:\; D_j\varphi|_{\Gamma_j}\,, \qquad j = 1,\ldots,J\,, \tag{4.4}$$

and the remainder R satisfies

$$\|R\|_{\mathcal{L}(C_*(\Gamma),C_*(\Gamma))} \;\le\; C\varepsilon\,, \tag{4.5}$$

where the constant C does not depend on ε.[2]

Note that the restriction of $D_j : C(\Gamma_j)/\mathbb{R} \to C(\Gamma_j)/\mathbb{R}$ is well defined, as the constant functions are eigenfunctions of D_j. Furthermore, for each $j = 1,\ldots,J$ the operator D_j is invertible on $C(\Gamma_j)/\mathbb{R}$ according to [3, Lemma 2.18]; in fact, from [2, Lemma 4.2] we even deduce that the operator norms of D_j and D_j^{-1} are independent of ε. We therefore conclude from (4.3) and (4.5) that

$$(E - K^N)^{-1} \;=\; D^{-1} + R' \tag{4.6}$$

for some operator $R' : C_*(\Gamma) \to C_*(\Gamma)$ with

$$\|R'\|_{\mathcal{L}(C_*(\Gamma),C_*(\Gamma))} \;\le\; C\varepsilon\,. \tag{4.7}$$

Inserting the factorization of Theorem 3.1, we can rewrite the quadratic form (2.6) as

$$Q[f] \;=\; \langle\, Af, (E - K^N)^{-1}\lambda Af\,\rangle\,, \tag{4.8}$$

and hence (4.6) yields

$$Q[f] \;=\; \sum_{j=1}^{m}\int_{\Gamma_j}(Af)(x)\,\psi_j(x)\;\mathrm{d}s \;+\; \langle\, Af, R'\lambda Af\,\rangle\,, \tag{4.9}$$

where

$$\psi_j \;=\; D_j^{-1}\big(\lambda Af\big)\big|_{\Gamma_j}\,. \tag{4.10}$$

We therefore turn next to investigating Af and λAf, respectively. As all points $x \in \Gamma_j$ converge to x_j as $\varepsilon \to 0$, with $|x - x_j| = O(\varepsilon)$, it follows that

$$(Af)(x) \;=\; \nu(x)\cdot\nabla u_{\mathbb{1}}(x) \;=\; \nu(x)\cdot\nabla u_{\mathbb{1}}(x_j) \;+\; r(x)\,, \qquad x \in \Gamma_j\,, \tag{4.11}$$

where the Taylor remainder $r \in C_\diamond(\Gamma)$ is uniformly bounded by

$$|r(x)| \;\le\; \|u_{\mathbb{1}}\|_{C^2(\overline{\Omega}_j)}\varepsilon\,, \qquad x \in \Gamma_j\,.$$

This can be further estimated by using the smoothing properties of A, i.e.,

$$\|r\|_{C(\Gamma)} \;\le\; C\varepsilon\|f\|_{H^{-s}(T)} \tag{4.12}$$

(cf., e.g., [17, Appendix]); the constant in (4.12) depends on s, but here we consider only fixed values of s. Accordingly, if we denote

$$\varphi_j(x) \;=\; (x - x_j)\cdot\nabla u_{\mathbb{1}}(x_j)\,, \qquad x \in \Gamma_j\,, \tag{4.13}$$

[2]Throughout, we use the letter C to denote a generic positive constant that is independent of ε, but may take different values at different occasions.

then

$$\|(\lambda Af)\big|_{\Gamma_j} - \varphi_j\|_{C(\Gamma_j)/\mathbb{R}} \le \|\lambda\|_{\mathcal{L}(C_\diamond(\Gamma),C_*(\Gamma))}\|r\|_{C(\Gamma)}\,. \tag{4.14}$$

(Note that φ_j can be shifted by any additive constant, as this is factored out in $C_*(\Gamma)$; hence we included x_j in the definition of φ_j mostly for a matter of taste—and to simplify the arguments below.)

It is fairly easy to see how λ is connected to the Neumann–Dirichlet operators

$$\lambda_j : C_\diamond(\partial O_j) \to C(\partial O_j)/\mathbb{R}$$

of the Laplacian in the reference domains O_j, $j = 1, \dots, J$, where

$$C_\diamond(\partial O_j) = \left\{ \chi \in C(\partial O_j) : \int_{\partial O_j} \chi \, \mathrm{d}s = 0 \right\},$$

and that

$$\|\lambda\|_{\mathcal{L}(C_\diamond(\Gamma),C_*(\Gamma))} = \varepsilon \max_{j=1,\dots,J} \|\lambda_j\|_{\mathcal{L}(C_\diamond(\partial O_j),C(\partial O_j)/\mathbb{R})}\,. \tag{4.15}$$

We therefore conclude from (4.14), (4.12), and (4.15) that

$$(\lambda Af)\big|_{\Gamma_j} = \varphi_j + O(\varepsilon^2)\,, \tag{4.16}$$

where the constant in the $O(\,\cdot\,)$-term depends only on the norm of f in $H^{-s}(T)$. Moreover, taking (4.13) into account, there holds

$$\|\lambda Af\|_{C_*(\Gamma)} \le C\varepsilon \|f\|_{H^{-s}(T)}\,, \tag{4.17}$$

as the gradient of $u_{\mathbb{1}}$ in the points x_j, $j = 1, \dots, J$, can again be estimated by the Neumann boundary values of $u_{\mathbb{1}}$ on T.

Inserting (4.10) and (4.16), as well as (4.7) and (4.17), into (4.9) we arrive at

$$Q[f] = \sum_{j=1}^{J} \int_{\Gamma_j} (Af)(x)(D_j^{-1}\varphi_j)(x) \, \mathrm{d}s + O(\varepsilon^3)\,,$$

where we have used the facts that the lengths of the boundaries Γ_j, $j = 1, \dots, J$, are of the order of ε, and that $\|D_j^{-1}\|$ as well as Af remain bounded as $\varepsilon \to 0$; cf. (4.11). Inserting (4.11) and (4.13) in the leading order term, we thus obtain

$$Q[f] = \sum_{j=1}^{J} \nabla u_{\mathbb{1}}(x_j) \cdot \left(\int_{\Gamma_j} \nu(x) D_j^{-1}(x - x_j) \, \mathrm{d}s \right) \nabla u_{\mathbb{1}}(x_j) + O(\varepsilon^3)\,, \tag{4.18}$$

because the remainder r in (4.11) satisfies (4.12) and φ_j is also bounded by some multiple of ε (cf. (4.13)), and because $|\Gamma_j| = O(\varepsilon)$. In (4.18) we take the gradient and the normal to be column vectors, whereas the variable x is considered to be a row vector; the term in big parentheses is then a two-by-two matrix, and the action of D_j^{-1} as well as the integration over Γ_j at the very end are to be taken componentwise.[3]

[3] Take note that there is also some abuse of notation in (4.18), as $D_j^{-1}(x - x_j)$ means that D_j^{-1} is applied to the function $\cdot - x_j$, the result of which is to be evaluated at x, followed by multiplication with $\nu(x)$ in (4.18). A similar comment applies to (4.19) and (4.20) below.

Transforming the integrals in (4.18) into integrals over ∂O_j by substituting the variables via

$$\widehat{x} \,=\, \frac{1}{\varepsilon}(x - x_j)\,, \qquad x \in \Gamma_j\,,$$

and using [2, Lemma 4.2] for the transformation of the double layer operators in (4.4), we obtain

$$\int_{\Gamma_j} \nu(x) D_j^{-1}(x - x_j)\, \mathrm{d}s \,=\, \varepsilon^2 \int_{\partial O_j} \nu(\widehat{x}) \Big(\frac{1}{2}\frac{1+\kappa_j}{1-\kappa_j}\, I - \widehat{K}_j \Big)^{-1} \widehat{x}\, \mathrm{d}\widehat{s}\,, \tag{4.19}$$

where we have introduced the double layer operators

$$(\widehat{K}_j \chi_j)(\widehat{x}) \,=\, \frac{1}{2\pi} \int_{\partial O_j} \frac{(\widehat{x} - \widehat{y}) \cdot \nu(\widehat{y})}{|\widehat{x} - \widehat{y}|^2}\, \chi_j(\widehat{y})\, \mathrm{d}\widehat{s}(\widehat{y})\,, \qquad \widehat{x} \in \partial O_j\,,$$

over ∂O_j, $j = 1, \ldots, J$. The two-by-two matrix

$$\int_{\partial O_j} \nu(\widehat{x}) \Big(\frac{1}{2}\frac{1+\kappa_j}{1-\kappa_j}\, I - \widehat{K}_j \Big)^{-1} \widehat{x}\, \mathrm{d}\widehat{s} \;=:\; M(\kappa_j, O_j) \,=\, \begin{bmatrix} a_j & c_j \\ c_j & b_j \end{bmatrix} \tag{4.20}$$

appearing in (4.19) is the so-called polarization tensor of Polya and Szegö; this matrix is symmetric and positive (resp., negative definite), depending on the sign of $1 - \kappa_j$; cf. [3] for its properties. For later use we also introduce two linear functionals of $M(\kappa_j, O_j)$, namely,

$$\alpha_j \,=\, a_j + b_j \qquad \text{and} \qquad \delta_j \,=\, b_j - a_j - 2\mathrm{i}c_j\,. \tag{4.21}$$

Inserting (4.19) and (4.20) into (4.18), we finally conclude that

$$Q[f] \,=\, \varepsilon^2 \sum_{j=1}^{J} \nabla u_{\mathbb{1}}(x_j) \cdot M(\kappa_j, O_j) \nabla u_{\mathbb{1}}(x_j) \,+\, O(\varepsilon^3)\,, \tag{4.22}$$

where the constant in the $O(\,\cdot\,)$-term depends only on the norm of f in $H^{-s}(T)$.

We mention that we can also estimate the bilinear form $\langle\, g, (\Lambda - \Lambda_{\mathbb{1}}) f \,\rangle$ for general $f, g \in H^{-s}_{\diamond}(T)$ in much the same way.

Concerning the backscatter data, we can now summarize our findings as follows.

THEOREM 4.1. *Let the inclusions Ω_j, $j = 1, \ldots, J$, of section 2 have the form $\Omega_j = x_j + \varepsilon O_j$ as in* (4.1). *Then the backscatter data* (2.7) *have a uniform expansion of the form*

$$b(\theta) \,=\, \varepsilon^2 \sum_{j=1}^{J} v(x_j, x_\theta) M(\kappa_j, O_j) v(x_j, x_\theta)^T \,+\, O(\varepsilon^3)\,, \qquad 0 \le \theta < 2\pi\,,$$

as $\varepsilon \to 0$, where $M(\kappa_j, O_j)$ is the polarization tensor of Polya and Szegö given by (4.20), *and*

$$v(x_j, x_\theta) \,=\, -\frac{1}{\pi} \left(\frac{|x_j - x_\theta|^2 x_\theta^\perp \,-\, 2(x_j \cdot x_\theta^\perp)(x_j - x_\theta)}{|x_j - x_\theta|^4} \right) \tag{4.23}$$

with $x_\theta^\perp = (-\sin\theta, \cos\theta)$.

Proof. Starting from (4.22), all we need to do is evaluate $v(x_j, x_\theta) = \nabla u_{\mathbb{1}}(x_j)^T$, where $u_{\mathbb{1}}$ is the reference potential corresponding to the input current $f = \delta'_{x_\theta}$. To this end, we recall from [16] that this reference potential is given by

$$u_{\mathbb{1}}(x) \,=\, -\frac{1}{\pi}\frac{x\cdot x_\theta^\perp}{|x-x_\theta|^2}\,,$$

and hence, it follows straightaway that

$$\nabla u_{\mathbb{1}}(x)^T \,=\, -\frac{1}{\pi}\left(\frac{|x-x_\theta|^2 x_\theta^\perp \,-\, 2(x\cdot x_\theta^\perp)(x-x_\theta)}{|x-x_\theta|^4}\right). \tag{4.24}$$

This yields the desired result. ∎

We mention that the fundamental formula (4.22)—or the corresponding result for $\langle\, g, (\Lambda-\Lambda_{\mathbb{1}})f\,\rangle$—is known; cf., e.g., [4, Theorem 1]. For $f, g \in \mathcal{L}^2_\diamond(T)$ the assertion follows from the results in [3], and the analysis there can be extended to the reduced regularity of f and g that is relevant for our Theorem 4.1. Nonetheless, we have preferred to include the above derivation to remain self-contained, partly also because we feel that this setting within the space of continuous functions on the boundaries of the inclusions allows for a somewhat simpler argument than within the Sobolev space context that is utilized in [3].

5. The holomorphic extension of the backscatter data. In this section we consider the backscatter data as a function of a complex variable on the unit circle, and hence, by some abuse of notation, we will further write $b(e^{\mathrm{i}\theta})$ instead of $b(\theta)$ as in (2.7). With this agreement it has been shown in [17] that the backscatter data extend as a holomorphic function to a certain subset of the complex plane.

THEOREM 5.1. *Let $\zeta^* = 1/\overline{\zeta}$ be the reflection of ζ at the unit circle, and likewise, let*

$$\Omega^* \,=\, \{\,\zeta\in\mathbb{C}\,:\,1/\overline{\zeta}\in\Omega\,\}$$

be the reflection of Ω. Then the backscatter data extend to a holomorphic function $b : \mathbb{C}\setminus(\overline{\Omega}\cup\overline{\Omega}^*) \to \mathbb{C}$ with

$$b(\zeta^*) \,=\, \overline{b(\zeta)}\,, \qquad \zeta\in\overline{B}\setminus\overline{\Omega}\,. \tag{5.1}$$

Moreover, if $0\notin\overline{\Omega}$, then b has a double root in $\zeta = 0$.

Proof. The fact that b has a holomorphic extension to $B\setminus\overline{\Omega}$ has been proved in [17], and this extension can be defined as follows. We identify $\xi\in\mathbb{C}$ with $x = (\operatorname{Re}\xi, \operatorname{Im}\xi)\in\Gamma$, and $\zeta\in\mathbb{C}$ with $x_\theta\in T$, respectively. Next we rewrite the gradient of the reference potential corresponding to $f = \delta'_{x_\theta}$ as

$$v(x, x_\theta) \,=\, \nabla u_{\mathbb{1}}(x)^T \,=\, (v_1, v_2)\,, \qquad x\in\Gamma\,,$$

where we omit the dependency of v_1 and v_2 on x and x_θ to simplify the notation. From (4.24) we conclude that $v(x, x_\theta)$ corresponds to the complex number

$$v_1 + \mathrm{i}v_2 \,=\, -\frac{1}{\pi}\frac{|\xi-\zeta|^2\mathrm{i}\zeta \,-\, 2\operatorname{Im}(\xi\overline{\zeta})(\xi-\zeta)}{|\xi-\zeta|^4}\,,$$

the real part of which is

$$v_1 = -\frac{\mathrm{i}}{2\pi}\frac{|\xi-\zeta|^2(\zeta-\overline{\zeta}) + 2\mathrm{i}\,\mathrm{Im}(\xi\overline{\zeta})(\xi+\overline{\xi}-\zeta-\overline{\zeta})}{|\xi-\zeta|^4}$$
$$= -\frac{\mathrm{i}}{2\pi}\frac{(\xi-\zeta)(\overline{\xi}-\overline{\zeta})(\zeta-\overline{\zeta}) + (\xi\overline{\zeta}-\overline{\xi}\zeta)(\xi+\overline{\xi}-\zeta-\overline{\zeta})}{(\xi-\zeta)^2(\overline{\xi}-\overline{\zeta})^2}.$$

Expanding this fraction by ζ^2, and using the fact that $|\zeta|^2 = 1$, we finally arrive at

$$v_1 = \frac{\mathrm{i}}{2\pi}\frac{(\overline{\xi}^2-1)\zeta^3 + 2(\xi-\overline{\xi})\zeta^2 + (1-\xi^2)\zeta}{(\xi-\zeta)^2(\overline{\xi}\zeta-1)^2}$$
$$= \frac{\mathrm{i}}{2\pi}\,\zeta\left(\frac{1}{(\zeta-\xi)^2} - \frac{1}{(\overline{\xi}\zeta-1)^2}\right). \tag{5.2}$$

In a similar fashion we rewrite the imaginary part v_2 as

$$v_2 = -\frac{1}{2\pi}\zeta\left(\frac{1}{(\zeta-\xi)^2} + \frac{1}{(\overline{\xi}\zeta-1)^2}\right). \tag{5.3}$$

Accordingly, if $\nu(x)$ is the outer normal at $x \in \Gamma$, we obtain

$$h(\zeta,x) := \nu(x)\cdot(v_1,v_2) = (A\delta'_{x_\theta})(x) \tag{5.4}$$

in (3.2). In (5.2)–(5.4) we still identify $x \in \Gamma$ with $\xi \in \mathbb{C}$ and have $\zeta = e^{\mathrm{i}\theta}$. Take note, however, that h extends as a holomorphic function of the variable ζ to $\mathbb{C}\setminus(\overline{\Omega}\cup\overline{\Omega}^*)$, as long as $x \in \Gamma$ is kept fixed; in what follows we will occasionally write $h(\zeta)$ instead of $h(\zeta,\,\cdot\,)$.

Inserting (5.4) into (4.8), we finally arrive at the representation

$$b(\zeta) = \langle\, h(\zeta), (E-K^N)^{-1}\lambda h(\zeta)\,\rangle \tag{5.5}$$

of the backscatter data, which provides the analytic extension of this function to $\zeta \in \mathbb{C}\setminus(\overline{\Omega}\cup\overline{\Omega}^*)$. As h satisfies the symmetry property (5.1), this property also carries over to b. Alternatively, (5.1) can be deduced from the reflection principle, as b is real valued on T.

From (5.5) it follows that

$$|b(\zeta)| \le \|(E-K^N)^{-1}\lambda\|_{\mathcal{L}(C_\diamond(\Gamma),C_*(\Gamma))}\|h(\zeta,\,\cdot\,)\|^2_{C_\diamond(\Gamma)}.$$

By virtue of (5.2)–(5.4),

$$\|h(\zeta,\,\cdot\,)\|_{C_\diamond(\Gamma)} = O(\zeta), \qquad \zeta\to 0,$$

provided that $0 \notin \overline{\Omega}$, and hence $b(\zeta) = O(\zeta^2)$ as $\zeta \to 0$ in this case; i.e., b has a double root in $\zeta = 0$. ∎

In view of Theorem 5.1 it is illuminating to reinterpret Theorem 4.1 in complex variables.

THEOREM 5.2. *Let the inclusions Ω_j, $j = 1,\dots,J$, of section 2 have the form $\Omega_j = x_j + \varepsilon O_j$ as in (4.1), where we identify $x_j = (x_{1j}, x_{2j})$ with the corresponding complex numbers $\xi_j = x_{1j} + \mathrm{i}x_{2j}$, $j = 1,\dots,J$. Further, we denote for a fixed value*

of $\varepsilon > 0$ the associated holomorphic extension of the backscatter data by b_ε. Then the rescaled functions $b_\varepsilon/\varepsilon^2$ converge to the rational function

$$F(\zeta) \,=\, \frac{1}{4\pi^2}\,\zeta^2 \sum_{j=1}^{J}\left(\frac{\delta_j}{(\zeta-\xi_j)^4} \,+\, \frac{\overline{\delta}_j}{(\overline{\xi}_j\zeta-1)^4} \,+\, \frac{2\alpha_j}{(\zeta-\xi_j)^2(\overline{\xi}_j\zeta-1)^2}\right) \tag{5.6}$$

as $\varepsilon \to 0$, uniformly on every compact subset of $\mathbb{C} \setminus \{\xi_j, \xi_j^* : j = 1, \ldots, J\}$, where α_j and δ_j are given by (4.21) *and depend on the Polya–Szegö polarization tensor $M(\kappa_j, O_j)$ of* (4.20).

Proof. We first observe that—for $\zeta \in \mathbb{C}$, and $x \in \mathbb{R}^2$ with associated $\xi \in \mathbb{C} \setminus \{\zeta, \zeta^*\}$—the vector $(v_1, v_2)^T$ of (5.4) is the gradient (with respect to x) of the complex-valued function

$$g(\zeta, x) \,=\, \frac{\mathrm{i}}{2\pi}\,\frac{\overline{\xi}\zeta^2 - \xi}{(\zeta-\xi)(\overline{\xi}\zeta-1)}\,, \qquad \xi \notin \left\{\zeta, \zeta^*\right\}.$$

It follows that we can rewrite (5.5) as

$$b_\varepsilon(\zeta) \,=\, \left\langle \frac{\partial}{\partial_x \nu} g(\zeta, x), (E - K^N)^{-1} \lambda \frac{\partial}{\partial_x \nu} g(\zeta, x) \right\rangle,$$

and as in section 4 we can thus conclude that

$$b_\varepsilon(\zeta) \,=\, \varepsilon^2 \sum_{j=1}^{J} \nabla_x g(\zeta, x_j) \cdot M(\kappa_j, O_j) \nabla_x g(\zeta, x_j) \,+\, O(\varepsilon^3)\,,$$

uniformly for ζ from any compact subset of $\mathbb{C} \setminus (\overline{\Omega} \cup \overline{\Omega}^*)$, and hence

$$\frac{b_\varepsilon(\zeta)}{\varepsilon^2} \,\to\, F(\zeta) \,=\, \sum_{j=1}^{J} \nabla_x g(\zeta, x_j) \cdot M(\kappa_j, O_j) \nabla_x g(\zeta, x_j)\,, \qquad \varepsilon \to 0\,.$$

By virtue of (5.2), (5.3) we have

$$\nabla_x g(\zeta, x_j) \,=\, \begin{bmatrix} v_1 \\ v_2 \end{bmatrix} \,=\, \frac{1}{2\pi}\left(\frac{\zeta}{(\zeta-\xi_j)^2}\begin{bmatrix} \mathrm{i} \\ -1 \end{bmatrix} \,-\, \frac{\zeta}{(\overline{\xi}_j\zeta-1)^2}\begin{bmatrix} \mathrm{i} \\ 1 \end{bmatrix}\right),$$

and hence the result follows at once from Theorem 4.1, since

$$\delta_j \,=\, \begin{bmatrix} \mathrm{i} \\ -1 \end{bmatrix}^T M(\kappa_j, O_j) \begin{bmatrix} \mathrm{i} \\ -1 \end{bmatrix}, \qquad \overline{\delta}_j \,=\, \begin{bmatrix} \mathrm{i} \\ 1 \end{bmatrix}^T M(\kappa_j, O_j) \begin{bmatrix} \mathrm{i} \\ 1 \end{bmatrix},$$

and

$$\alpha_j \,=\, -\begin{bmatrix} \mathrm{i} \\ 1 \end{bmatrix}^T M(\kappa_j, O_j) \begin{bmatrix} \mathrm{i} \\ -1 \end{bmatrix}. \qquad \square$$

We remark that the poles of F are precisely the locations ξ_j of the inclusions, as well as their reflections at the unit circle.

Remark 5.3. It is interesting to note that each location ξ_j gives rise to a fourth order pole of F, except for the case when the polarization tensor $M(\kappa_j, O_j)$ is a multiple of the identity matrix—the latter being true, e.g., for circular inclusions. In

that special instance, the parameter δ_j of (4.21) vanishes, and hence F has only a second order pole in ξ_j.

Remark 5.4. Another important aspect of Theorem 5.2 concerns circular inclusions that are located in the center of the unit disk. For those inclusions we not only have that $\delta_j = 0$ in (5.6) but also that the second order pole in $\xi_j = 0$ cancels with the factor ζ^2 in front of the sum in (5.6). In other words, circular inclusions in the origin do not appear as poles of F. This reflects the fact that the backscatter of a single circular inclusion is constant.

6. Locating small inclusions from backscatter data. According to Theorem 5.2 the backscatter data can be well approximated by rational functions when the inclusions are reasonably small. It is tempting to use this as the basis for a numerical algorithm to locate the inclusions, even when they have finite extent. Similar algorithms have been used before in impedance tomography, e.g., in [6, 7, 13, 21], or for inverse source problems for the Poisson equation; cf. [8, 18].

We are therefore looking for a rational function $r : \mathbb{C} \to \mathbb{C}$ that approximates the given backscatter data on the unit circle; moreover, motivated by the fact that the backscatter is real-valued, and by (5.6), we impose that r be symmetric with respect to the unit circle, i.e.,

$$r(\zeta^*) = \overline{r(\zeta)}\,, \qquad \zeta \in \mathbb{C}\,, \tag{6.1}$$

and has a double root at $\zeta = 0$ (and hence at infinity as well). An appropriate concept for the design of such rational functions are the so-called Laurent–Padé approximations that have been introduced by Gragg and Johnson [11].[4]

Let us assume that the backscatter function is given as a Laurent series,

$$b(\zeta) = \sum_{\nu=-\infty}^{\infty} \beta_\nu \zeta^\nu\,, \tag{6.2}$$

which converges in a neighborhood of the unit circle. Then, for $m \geq 2$, the $(m-2, m)$-Laurent–Padé approximation r_m of b, if it exists, is a fraction of two finite Laurent series of Laurent degrees $m-2$ and m, respectively, or, in other words, r_m is a rational function with (polynomial) denominator degree $2m$ and numerator degree $2m-2$. In particular, r_m has a double zero at the origin and at infinity, the same property that the rational function F of Theorem 5.2 has. Moreover, as b is symmetric with respect to the unit circle, i.e., as

$$\beta_{-\nu} = \overline{\beta_\nu}\,, \qquad \nu \in \mathbb{Z}\,, \tag{6.3}$$

it follows that r_m is symmetric, too; i.e., $r = r_m$ satisfies (6.1). Finally, among all these rational functions, r_m is the only one whose Laurent coefficients are chosen so as to match those of b for $\nu = -2m+2, \ldots, 2m-2$.

The computation of r_m is fairly easy: essentially, it boils down to solving one single $m \times m$ Hankel system of linear equations; see the appendix or [5, 11] for details. As in all Padé approximations, however, r_m may not exist for certain $m \geq 2$. Even when it exists, there may be a catch that—despite its construction—its Laurent coefficients fail to match those of b. This latter failure is connected to the notion of *stable*

[4]Here we follow the original terminology from Gragg and Johnson; beware of the fact that Baker and Graves-Morris in their commendable reference work [5] refer to these approximations as Padé–Laurent approximations and reserve the name Laurent–Padé for something different.

Padé approximations introduced by Trefethen and Gutknecht [26] and can easily be detected at runtime.

Take note that the symmetry of r_m and b is equivalent to the fact that these functions are real-valued along the unit circle. Also observe that the Laurent coefficients β_ν of (6.2) are nothing else than the Fourier coefficients of the given data $b(e^{\mathrm{i}\theta})$, considered as a periodic function of $\theta \in [0, 2\pi]$. In other words, the rational function r_m is designed to be a low-frequency approximation of b along the unit circle, and hence the computation of r_m has some inherent regularizing effect for moderate values of m; reasonable choices of m can be determined visually by counting the Fourier coefficients above the noise level; cf. subsection 7.4.

The rational function r_m is a good candidate for approximating b, not only on T, but also in compact subsets of $\mathbb{C} \setminus (\overline{\Omega} \cup \overline{\Omega}^*)$. It has to be emphasized, though, that the number of corresponding analytical results is rather scarce. Still, one may hope that most of the poles of r_m will happen to lie within or nearby the inclusions. We emphasize that the symmetry of r_m implies that its poles come in pairs, symmetrically reflected at the unit circle; accordingly, exactly m poles of r_m will lie within the unit circle. More precisely, as long as there occur no multiple poles (which is the generic case in a real computation), r_m admits a partial fraction expansion of the form

$$r_m(\zeta) = \lambda_0 + \sum_{k=1}^{m} \Big(\frac{\lambda_k}{\zeta - \zeta_k} + \frac{\overline{\lambda}_k \zeta}{1 - \zeta \overline{\zeta}_k} \Big), \tag{6.4}$$

with poles ζ_k and ζ_k^*, where we enumerate the poles in such a way that ζ_k, $k = 1, \ldots, m$, are the ones within the unit disk. Some of these can have very small residues $\lambda_k \in \mathbb{C}$, though, in which case they may well be considered spurious and should be discarded eventually. We consider the remaining poles as approximate locations of the inclusions, and in view of Theorem 5.2, we expect that, the smaller the inclusions, the more accurate the approximations.

7. Numerical results. In the following we present numerical case studies using several phantoms with a variety of inclusions of different shapes, sizes, and conductivities. For these examples backscatter data at 768 equidistant grid points on the unit circle have been generated by solving the boundary value problems (2.3) with a boundary element code. Numerical results will be presented under different assumptions on the number and the quality of data that are used: In fact, each reconstruction is computed from n values $b(e^{\mathrm{i}\theta_\ell})$ of the backscatter at equidistant boundary angles $\theta_\ell = 2\ell\pi/n$, but n will vary considerably in what follows. As we discuss in more detail in subsection 7.2, an FFT of the given data provides accurate approximations $\widehat{\beta}_\nu$ of the Laurent coefficients β_ν of (6.2), at least for moderate values $|\nu| \le \nu^*$, where the appropriate bound $\nu^* \ll n/2$ depends on various parameters, and will be estimated below; cf. (7.2).

We start with an idealistic setting, where we use "almost continuous" noiseless data; that is, n is very large; subsequently, we turn to more discrete data sets, both with and without noise.

7.1. Idealistic setting. To begin with we illustrate the potential of our method for a first example with inclusions of considerable extent, utilizing for the reconstruction all $n = 768$ boundary angles for which backscatter data have been simulated. Figure 7.1 shows the backscatter on the left and the poles of the corresponding $(m-2, m)$-Laurent–Padé approximation r_m for $m = 64$ on the right. Only those

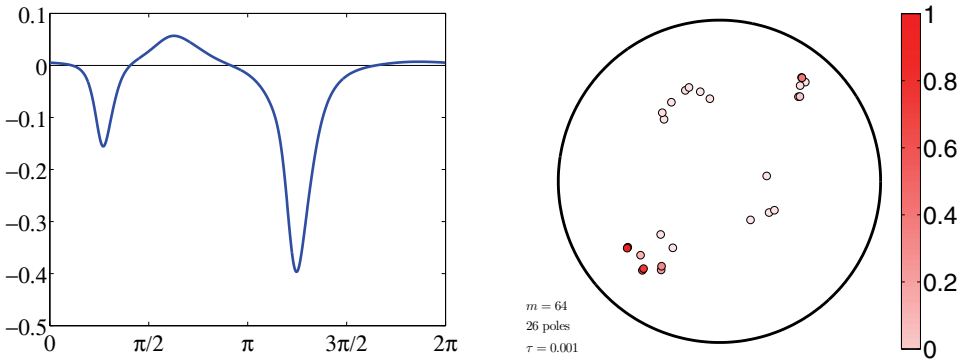

FIG. 7.1. *Backscatter data (left) as a function of θ, and reconstructed poles (right) in the unit disk; no noise, $m = 64$.*

26 poles in the unit disk are shown (as spots), whose residues (relative to the maximal residue) are above a threshold $\tau = 10^{-3}$. These spots are color coded to visualize the relative magnitudes of the corresponding residues; the darker the spot, the more pronounced the pole is on a scale between zero and one, as indicated by the color bar. Note that some of these poles are almost multiple poles, as the corresponding spots overlap.

The reconstruction shows two well-separated clusters in the NE and SW parts of the disk, obviously corresponding to the significant negative deflections of the backscatter data near $\theta = \pi/4$ and $5\pi/4$, respectively; these two clusters most likely correspond to one inclusion each, with conductivities greater than one. The somewhat C-shaped arrangement of poles in the NNW part of the disk is due to the positive peak of the backscatter data near $\theta = 2\pi/3$. The remaining four poles between the center, and the east of the disk indicate that there may be another inclusion over there—in fact, as the backscatter changes sign twice between $3\pi/2$ and $\pi/6$, there is some evidence of another inclusion in that part of the disk with conductivity below the background conductivity.

Figure 7.2 resolves this little puzzle by showing the true inclusions (as solid lines) in the right-hand side plot. It is fascinating to see that the poles not only locate the inclusions, but also provide very decent shape information. For this example we have fixed the conductivities to be $\kappa_j = 2$, 0.5, 10, and 0.5, respectively (in counter clockwise orientation, starting with the inclusion in the NE); except for the sign of $\kappa - 1$, however, we see no obvious possibility yet of extracting more detailed information about the conductivities with our approach.

On the left-hand side of Figure 7.2 one can see that the approximation r_m on the unit circle (the dashed line, as compared to the solid backscatter line) is a perfect match of the given data, as it is almost impossible to distinguish the two curves visually; in fact, the relative error between these two functions has about the order of machine precision.

Strictly speaking, this experiment goes far beyond the theory that has been developed in the previous paragraphs, as the inclusions are not really small, at least not in the sense considered in Theorem 5.2. We therefore provide the result of a second experiment, for which we have scaled down the inclusions by a factor of four; the corresponding phantom, backscatter, and reconstruction are shown in Figure 7.3. We emphasize the different scale of the vertical axis in the backscatter plot: As predicted

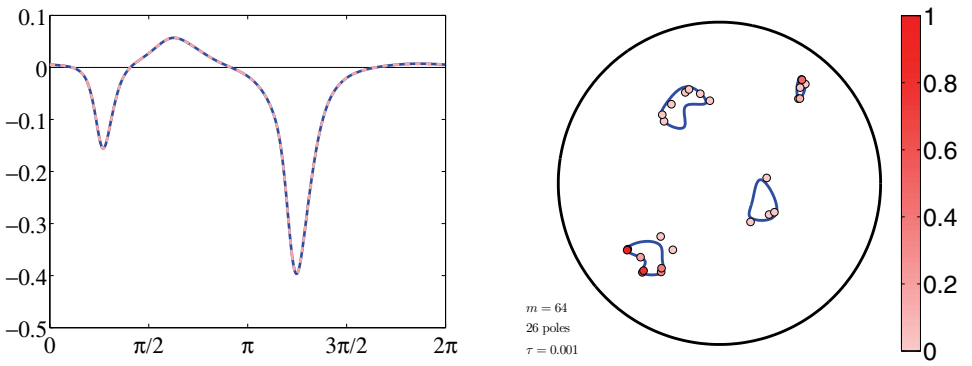

FIG. 7.2. *Same as Figure* 7.1*, but including the approximation* r_{64} *on the left (dashed line), and the true inclusions on the right.*

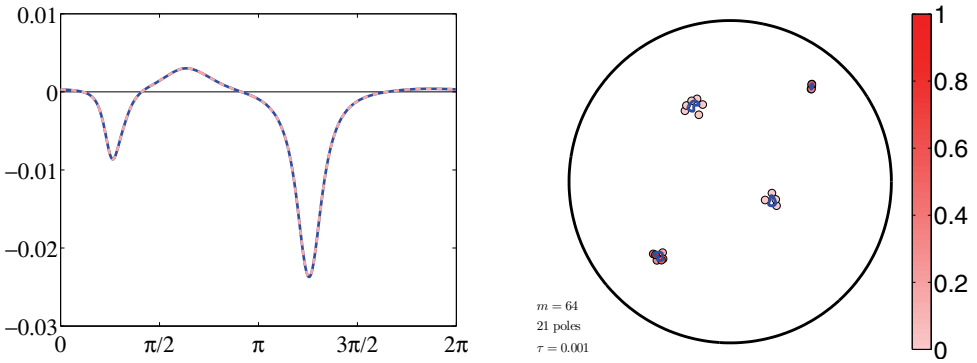

FIG. 7.3. *Similar to Figure* 7.2*, but with inclusions that have been reduced by a factor of four.*

by Theorem 5.2, the backscatter in Figure 7.3 (left) is, roughly, by a factor of 16 smaller than the one in Figure 7.2 (left). To facilitate the appreciation of the reconstruction in the right-hand side plot of Figure 7.3, this time the inclusions are plotted on top of the poles, the latter providing very well the locations of all four inclusions.

7.2. Discrete data, no noise. The setting from subsection 7.1 is unrealistic in that real data will hardly have that many high-frequency information. Instead, a realistic setting may consist of $n = 32$, or at best, $n = 64$ equidistant data points. A rough calculation based on the assumption that the coefficients of the Laurent series (6.2) behave like

$$|\beta_\nu| \approx c\rho^{|\nu|}, \qquad \nu \in \mathbb{Z}, \tag{7.1}$$

where $c > 0$ and $\rho = \sup\{|\zeta| : \zeta \in \Omega\}$ (cf. [20]), indicates that the discrete Fourier coefficients $\widehat{\beta}_\nu$ approximate the Laurent coefficients β_ν with a relative error of about

$$\frac{|\widehat{\beta}_\nu - \beta_\nu|}{|\beta_\nu|} \lesssim \rho^{n-2|\nu|}, \qquad |\nu| \le n/2;$$

cf., e.g., Henrici [19, p. 20]. If we refrain from using Fourier coefficients whose relative error is above some tolerance ω, then the above rule of thumb constrains us to using

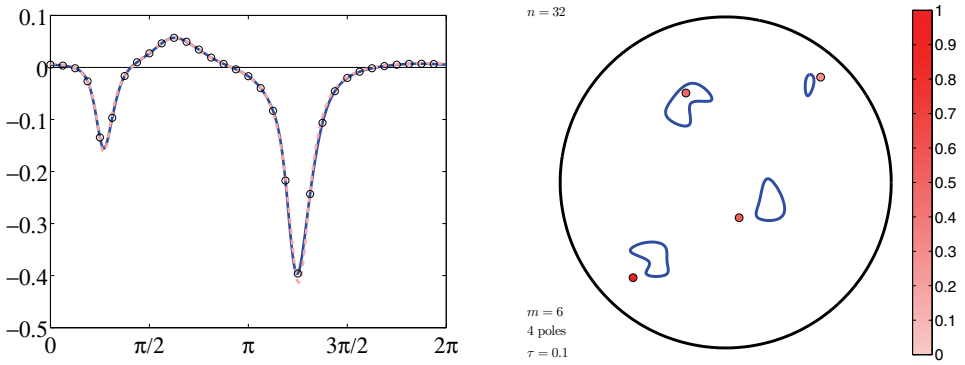

FIG. 7.4. *Numerical results with only $n = 32$ data samples and Laurent degree $m = 6$.*

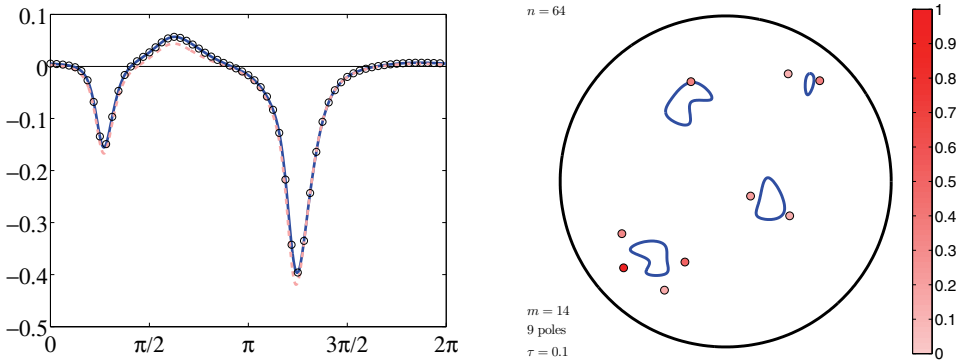

FIG. 7.5. *Numerical results with $n = 64$ data samples and Laurent degree $m = 14$.*

only those coefficients with indices $|\nu| \le \nu^* = (n-d)/2$, where $d = \log\omega/\log\rho$, and it thus follows that the parameter m of the $(m-2,m)$-Laurent–Padé approximation should satisfy $2m-2 \le \nu^*$ (cf. section 6), i.e.,

$$m \le \frac{\nu^*}{2} + 1 = \frac{n-d}{4} + 1\,. \tag{7.2}$$

The parameter ρ can be estimated by replacing β_ν by $\widehat{\beta}_\nu$ in (7.1), and in the example of Figure 7.1 this yields $\rho \approx 0.8$, and hence $d \approx 10$ for $\omega = 0.1$.

We therefore should not drive m above six in that example, when $n = 32$ data samples are to be used, which in turn means that only four to six poles will carry realistic information. Figure 7.4 shows the corresponding result for the $(m-2,m)$-Laurent–Padé approximation r_m with $m = 6$. Note that we have increased the value of τ to 0.1 for this reduced data set, and two poles have been eliminated because of that, since their residues failed to pass the nonnegligibility test. The four remaining poles pick one inclusion each—although the one in the east has barely been localized.

The left-hand side plot of Figure 7.4 shows the full backscatter data as solid line, whereas the discrete backscatter samples that are used for the reconstruction are highlighted as small circles. The rational approximation of the data is again included as a dashed line. As can be seen, this approximation slightly overshoots the global minimum of the backscatter near $\theta = 5\pi/4$, and that is why the corresponding pole is somewhat too close to the boundary of the disk.

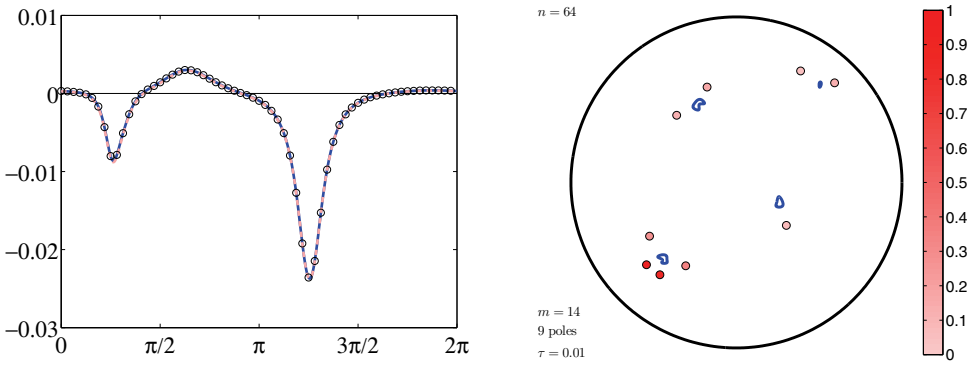

FIG. 7.6. *Numerical results with $n = 64$ data samples for the example with small inclusions.*

Concerning $n = 64$ equidistant backscatter samples, we refer to Figure 7.5 for the corresponding reconstruction. Here, we choose $m = 14$ according to the estimate (7.2), using the same value d as before. In this case 9 out of 14 poles pass our residue filter, and all poles provide fair approximations of the true locations. We hasten to remark, though, that there is a chance that reasonable choices of m yield misleading results; for this data set, for example, we obtain a relevant pole right in the center of the three inclusions in the NE part of the disk when we select $m = 13$ instead of $m = 14$. Accordingly, care has to be taken when interpreting these numerical results. In a real computation, one should try various Laurent degrees when appropriate to observe "stable" clusters of poles over a certain range of admissible values for m.

Again, we also investigate the impact of the size of the inclusions on the outcome of the method, and we reconsider the example from Figure 7.3 with the tiny inclusions. Figure 7.6 presents the corresponding numerical result for $n = 64$ backscatter samples. In view of Theorem 5.2, the estimate for ρ in (7.1) should roughly be the same as before so that we can use the same degree $m = 14$ for the rational approximation as in the previous case. A comparison of Figure 7.6 with Figure 7.3 reveals that the poles are affected quite a bit by the reduced number of data, and that the localization of the inclusions is no more better than for the larger ones.

Again, we have triggered the quality of the reconstruction by choosing the threshold $\tau = 10^{-2}$ somewhat smaller than before; with $\tau = 0.1$, as in the previous example, all three poles in the eastern half of the disk would have been eliminated, with the effect that the rational approximation $r_m(e^{\mathrm{i}\theta})$ would have been almost constant for $\theta \in (-\pi/2, \pi/2)$, thus failing to approximate the two local extrema of the backscatter on that part of the circle.

We omit the corresponding result for $n = 32$ data points; the reconstruction is somewhat worse in that case, but still useful.

7.3. The impact of the conductivity. As another test case we consider an example with two identical inclusions, having the same distance to the boundary, but differing in their conductivities. For this setup we have run two experiments, where one of the conductivities, $\kappa = 0.5$, has been kept fixed, while two different conductivities, namely $\kappa = 0.8$ in the first run (Figure 7.7) and $\kappa = 0.95$ in the second one (Figure 7.8), have been assigned to the other inclusion; recall that $\sigma = 1$ is the background conductivity, so that the second inclusion has a reduced contrast in the second test case.

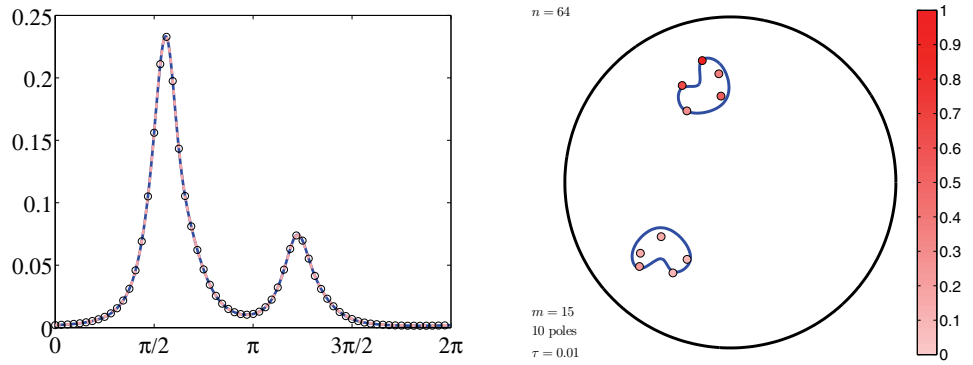

FIG. 7.7. *Two inclusions with conductivities* $\kappa = 0.5$ *(top) and* $\kappa = 0.8$ *(bottom), respectively;* $n = 64$ *data samples.*

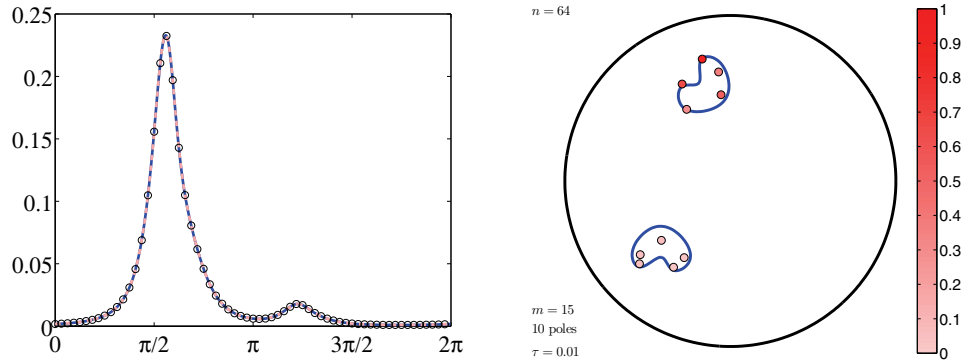

FIG. 7.8. *Two inclusions with conductivities* $\kappa = 0.5$ *(top) and* $\kappa = 0.95$ *(bottom), respectively;* $n = 64$ *data samples.*

As expected, the second peak of the backscatter—corresponding to the inclusion in the SW—is disappearing with diminishing contrast in the conductivity; however, it can be seen from the good quality of the approximation $r_m \approx b$, as well as from the computed poles in the right-hand side plots, that the rational approximation can still take care of that peak, as long as it is discernible. Of course, with reduced contrast, the absolute values of the associated residuals λ_k in the partial fraction expansion (6.4) of r_m drop down, as can be seen from the intensity of the spots in the right-hand side plots. Accordingly, if we would increase our threshold to $\tau = 0.1$, only three of the SW poles would have survived in the first test case, while none of them would have jumped over this threshold in the second test case, where $\kappa = 0.95$. (Again, a plot of r_m would then reveal that the rational approximation fails to trace the second bump of the backscatter data, calling for a smaller threshold parameter instead.)

7.4. Discrete data with noise. As our problem is extremely ill-posed, it doesn't come as a surprise that the situation changes for the worse when the data are perturbed by "noise"; for our experiments we choose uniformly distributed entries with absolute values below some parameter δ as a realistic noise model. In what follows we describe how we regularize our code for noisy data.

In the presence of noise, less Fourier coefficients carry relevant information, and

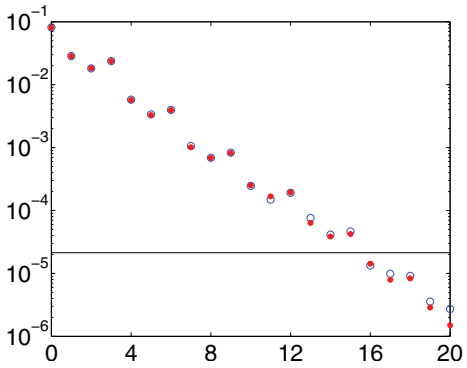

FIG. 7.9. *Discrete Fourier coefficients in the presence of noise* ($\delta = 10^{-3}$)*; see text for explanations.*

we therefore incorporate a first regularization of the problem by reducing the number ν^* of discrete Fourier coefficients to be used for the Padé approximation. We illustrate this procedure for the example of Figure 7.7, where the two identical inclusions have conductivities $\kappa = 0.5$ and $\kappa = 0.8$, respectively. We use the same number of $n = 64$ data points and simulate noise with noise level $\delta = 10^{-3}$, which is a few permille of the maximal backscatter, but just slightly below the minimal backscatter, which is about $1.5 \cdot 10^{-3}$; cf. the left-hand plot of Figure 7.7.

Figure 7.9 shows—as a function of ν—the squared (absolute) Laurent coefficients $|\beta_\nu|^2$ and their approximations $|\widehat{\beta}_\nu|^2$ as filled dots, and open circles, respectively. The horizontal solid line indicates the expected squared Euclidean norm of the noise, which is $(n/3)\delta^2 \approx 2 \cdot 10^{-5}$. Fourier coefficients corresponding to circles below that line may be largely corrupted by noise, and for this reason should not be considered reliable. As can be seen from that, only the Laurent coefficients β_ν with $|\nu| \le 15$ can be retrieved with sufficient accuracy for this particular noise sample.

Fixing the cut-off to be $\nu^* = 14$ we go on to choose $m = 8$ for the Laurent–Padé approximation according to the left-hand equation in (7.2). Still, we need to modify our criterion according to which we keep or delete terms in the partial fraction expansion (6.4) of r_m. Remember that, so far, we have neglected only poles whose residues have been relatively small. The magnitude of a residue, however, is difficult to link to the noise level in the data, and so this criterion may not be sufficient for noisy data. Therefore, we also evaluate each individual term of the partial fraction expansion (6.4) at the n boundary points and remove those terms whose boundary values are below the expected value of the squared norm of the noise, i.e.,

$$\sum_{\ell=1}^{n} \Big(2 \operatorname{Re} \frac{\lambda_k}{e^{\mathrm{i}\theta_\ell} - \zeta_k} \Big)^2 \; < \; \frac{n}{3}\, \delta^2 \,, \qquad k \in \{1, \ldots, m\} \,.$$

Note that this approach resembles the well-known discrepancy principle from the ill-posed problems literature (cf., e.g., [9]), which states that approximate solutions are to be improved just until the data fit is within the level of the noise. This modification of our code provides a second regularization of the problem.

Figure 7.10 displays the computed locations of the inclusions, together with the noisy input data; as can be seen from the circles in the left-hand side plots, i.e., the given data, the noise affects the data mostly in that part of the circle that is far from

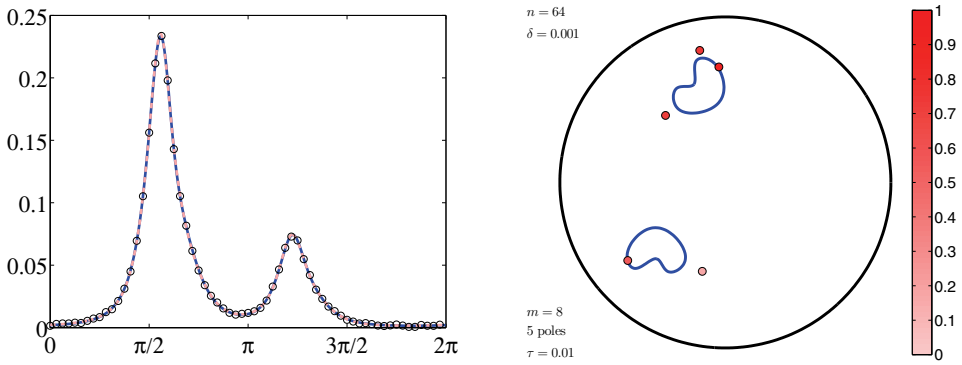

FIG. 7.10. *Numerical results for* $n = 64$ *noisy data samples;* $\delta = 10^{-3}$.

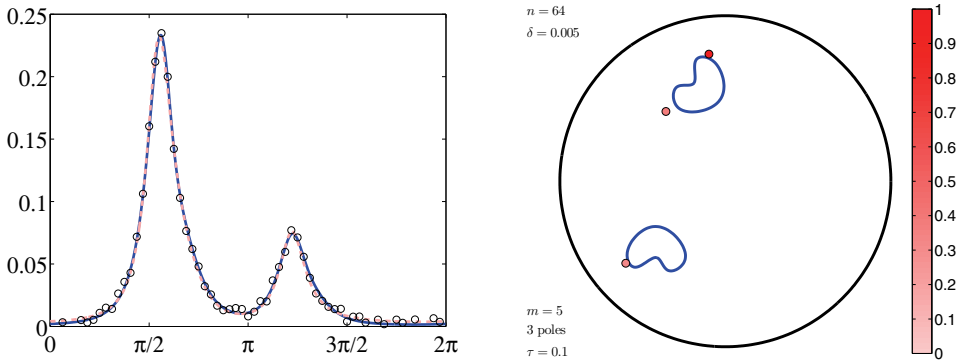

FIG. 7.11. *Numerical results for* $n = 64$ *noisy data samples;* $\delta = 5 \cdot 10^{-3}$.

the inclusions, and our regularization techniques successfully prevent the appearance of spurious poles in that area.

When we increase the noise level by a factor of five, i.e., $\delta = 5 \cdot 10^{-3}$, then the $n = 64$ data points exhibit more serious oscillations; see the left-hand plot in Figure 7.11. In particular, wiggles in the backscatter data do also show up in that part of the circle that is between the two inclusions. These perturbations affect the rational approximations more severely than the oscillations at the opposite part of the boundary. To compensate for that, we have increased the residue threshold somewhat further to $\tau = 0.1$, accepting that this reduces the ability to detect objects with lower contrast; cf. subsection 7.3. Finally, because the noise is stronger, less Fourier coefficients are sufficiently accurate, and therefore we have to decrease the degree of the Pade approximations to $m = 5$, or $m = 6$ at most. As can be seen in Figure 7.11 this leaves us with only three poles that satisfy all our safeguards—but these poles suffice to locate the two inclusions fairly well.

Taking the strong perturbations of the noisy backscatter data in Figure 7.11 into account, it is evident that different noise samples may affect the reconstructions in various ways. We therefore conclude by showing in Figure 7.12 reconstructions for eight different noise samples, using the same noise level as before, i.e., $\delta = 0.5 \cdot 10^{-3}$. We observe that two out of the three poles shown in Figure 7.11 are fairly robust, one for each of the inclusions. The third pole meanders between the two inclusions or may split into another pair of poles.

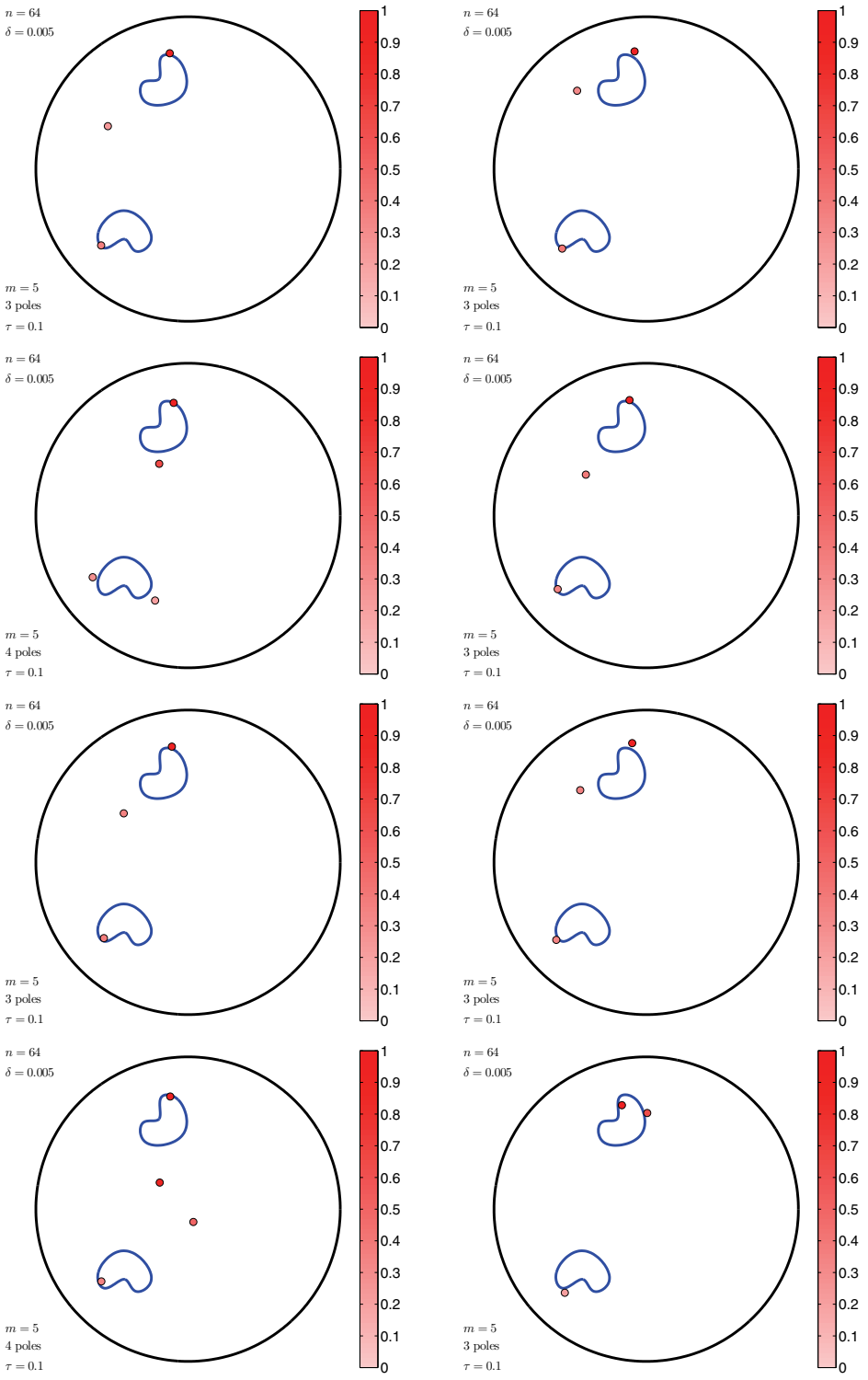

FIG. 7.12. *Numerical results for different noisy data samples, each with noise level* $\delta = 5 \cdot 10^{-3}$.

8. Concluding remarks. We have shown that the backscatter of a finite union of small inclusions within a homogeneous disk can be well approximated by rational functions, and that the poles of these functions can be used to locate the inclusions. We also have presented a corresponding algorithm using Laurent–Padé approximations and developed safeguards to stabilize (regularize) the algorithm in the presence of noise. Our numerical results demonstrate that the method is not limited to very small inclusions but is applicable also when the inclusions have nonnegligible size.

In our numerical examples we have restricted ourselves to (ℓ, m)-Laurent–Padé approximations with $\ell = m - 2$ because of their double root near zero (and infinity). However, numerical test runs with $\ell = m$ gave similar results; we mention, though, that when $\ell = m$, the Padé algorithm requires 2×2 further Fourier coefficients, namely $\beta_{\pm(2m-1)}$ and $\beta_{\pm 2m}$. Other rational approximation schemes, such as those based on the rational Carathéodory–Fejér method (resp., the Adamjan–Arov–Kreĭn theory; cf. [6, 7, 12, 25]), may have further advantages.

The stability of the algorithm with respect to noise has been exemplified for a test problem with two inclusions. Since backscatter data are relative data, the impact of noise may be disastrous when an inclusion has little influence on the data, be it because (i) the contrast in conductivity is low, (ii) the inclusion is small, or (iii) the inclusion is near the center of the object. This, of course, reflects the ill-posedness of the problem.

Finally we mention that, in principle, it should also be possible to extend the techniques from [18] to extract shape information about the inclusions from the residues of the poles and to refine such a first guess by some Newton iteration afterwards. This is left for future research.

Appendix. Computation of the Laurent–Padé approximation. We conclude with a brief description of the computation of the $(m-2, m)$-Laurent–Padé approximation r_m of the backscatter. For the theoretical background we refer to [5, sect. 7.4].

As the backscatter is real-valued over T, the Laurent–Padé approximation r_m assumes the form

$$r_m(\zeta) \;=\; \frac{p(\zeta)\overline{q}(1/\zeta) \,+\, \overline{p}(1/\zeta)q(\zeta)}{q(\zeta)\overline{q}(1/\zeta)}\,, \tag{A.1}$$

where the polynomials p and q are given by

$$p(\zeta) \;=\; \sum_{\nu=0}^{m} p_\nu \zeta^\nu \qquad \text{and} \qquad q(\zeta) \;=\; \sum_{\nu=0}^{m} q_\nu \zeta^\nu\,, \tag{A.2}$$

and the polynomials $\overline{p}$ and $\overline{q}$ are obtained from p and q by taking the complex conjugates of their respective expansion coefficients.

Given the Laurent coefficients β_ν of the backscatter (cf. (6.2)), the coefficients q_ν, $1 \le \nu \le m$, of q are obtained from the linear system

$$\begin{bmatrix} \beta_{-1} & \beta_0 & \dots & \beta_{m-2} \\ \beta_0 & \beta_1 & & \vdots \\ \vdots & & \ddots & \\ \beta_{m-2} & \dots & & \beta_{2m-3} \end{bmatrix} \begin{bmatrix} q_m \\ q_{m-1} \\ \vdots \\ q_1 \end{bmatrix} \;=\; - \begin{bmatrix} \beta_{m-1} \\ \beta_m \\ \vdots \\ \beta_{2m-2} \end{bmatrix}, \tag{A.3}$$

and q_0 is set to be $q_0 = 1$. Subsequently, the coefficients p_ν are given by

$$\begin{bmatrix} p_m \\ p_{m-1} \\ \vdots \\ p_1 \\ p_0 \end{bmatrix} = \begin{bmatrix} \beta_0/2 & \beta_1 & \cdots & \cdots & \beta_m \\ 0 & \beta_0/2 & \ddots & & \vdots \\ \vdots & \ddots & \ddots & \ddots & \vdots \\ \vdots & & \ddots & \ddots & \beta_1 \\ 0 & 0 & \cdots & 0 & \beta_0/2 \end{bmatrix} \begin{bmatrix} q_m \\ q_{m-1} \\ \vdots \\ q_1 \\ 1 \end{bmatrix}. \tag{A.4}$$

In effect, the computation of r_m requires all Laurent coefficients β_ν with $|\nu| \le 2m-2$; Laurent coefficients with negative indices are redundant, though; cf. (6.3).

We mention that it is obvious from (A.2) that the denominator in (A.1) is a Laurent polynomial of degree m, whereas it is less obvious that the numerator Laurent polynomial in (A.1) has a reduced degree $m-2$; see [5] for a proof. Finally, we remark that r_m fails to be well defined when the Hankel matrix in (A.3) is singular.

REFERENCES

[1] A. Adler, R. Gaburro, and W. Lionheart, *Electrical Impedance Tomography*, in Handbook of Mathematical Methods in Imaging, O. Scherzer, ed., Springer, New York, 2011, pp. 599–654.

[2] H. Ammari, R. Griesmaier, and M. Hanke, *Identification of small inhomogeneities: Asymptotic factorization*, Math. Comp., 76 (2007), pp. 1425–1448.

[3] H. Ammari and H. Kang, *Polarization and Moment Tensors with Applications to Inverse Problems and Effective Medium Theory*, Springer, New York, 2007.

[4] H. Ammari and H. Kang, *Expansion Methods*, in Handbook of Mathematical Methods in Imaging, O. Scherzer, ed., Springer, New York, 2011, pp. 447–499.

[5] G. A. Baker and P. Graves-Morris, *Padé Approximants*, 2nd ed., Cambridge University Press, Cambridge, UK, 1996.

[6] L. Baratchart, A. Ben Abda, F. Ben Hassen, and J. Leblond, *Recovery of pointwise sources or small inclusions in 2D domains and rational approximation*, Inverse Problems, 21 (2005), pp. 51–74.

[7] L. Baratchart, J. Leblond, F. Mandréa, and E. B. Saff, *Identification of conductivity imperfections of small diameter by boundary measurements: Continuous dependence and computational reconstruction*, Inverse Problems, 15 (1999), pp. 79–90.

[8] A. El Badia and T. Ha-Duong, *An inverse source problem in potential analysis*, Inverse Problems, 16 (2000), pp. 651–663.

[9] H. W. Engl, M. Hanke, and A. Neubauer, *Regularization of Inverse Problems*, Kluwer, Dordrecht, The Netherlands, 1996.

[10] A. Friedman and M. S. Vogelius, *Identification of small inhomogeneities of extreme conductivity by boundary measurements: A theorem on continuous dependence*, Arch. Rational Mech. Anal., 105 (1989), pp. 299–326.

[11] W. B. Gragg and G. D. Johnson, *The Laurent–Padé table*, in Information Processing 74, (Proc. IFIP Congress, Stockholm, 1974), North-Holland, Amsterdam, 1974, pp. 632–637.

[12] M. H. Gutknecht, *Rational Carathéodory-Fejér approximation on a disk, a circle, and an interval*, J. Approx. Theory, 41 (1984), pp. 257–278.

[13] M. Hanke, *On real-time algorithms for the location search of discontinuous conductivities with one measurement*, Inverse Problems, 24 (2008), 045005.

[14] M. Hanke and M. Brühl, *Recent progress in electrical impedance tomography*, Inverse Problems, 19 (2003), pp. S65–S90.

[15] M. Hanke, B. Harrach, and N. Hyvönen, *Justification of point electrode models in electrical impedance tomography*, Math. Models Methods Appl. Sci., 21 (2011), pp. 1395–1413.

[16] M. Hanke, N. Hyvönen, and S. Reusswig, *An inverse backscatter problem for electric impedance tomography*, SIAM J. Math. Anal., 41 (2009), pp. 1948–1966.

[17] M. Hanke, N. Hyvönen, and S. Reusswig, *Convex backscattering support in electric impedance tomography*, Numer. Math., 117 (2011), pp. 373–396.

[18] M. Hanke and W. Rundell, *On rational approximation methods for inverse source problems*, Inverse Probl. Imaging, 5 (2011), pp. 185–202.
[19] P. Henrici, *Applied and Computational Complex Analysis*, Vol. 3, John Wiley, New York, 1986.
[20] S. Hollborn, *Reconstructions from backscatter data in electric impedance tomography*, Inverse Problems, 27 (2011), 045007.
[21] H. Kang and H. Lee, *Identification of simple poles via boundary measurements and an application of EIT*, Inverse Problems, 20 (2004), pp. 1853–1863.
[22] R. Kress, *Linear Integral Equations*, 2nd ed., Springer, Berlin, 1999.
[23] R. Kress and L. Kühn, *Linear sampling methods for inverse boundary value problems in potential theory*, Appl. Numer. Math., 43 (2002), pp. 161–173.
[24] O. A. Ladyzhenskaya, *The Boundary Value Problems of Mathematical Physics*, Springer, New York, 1985.
[25] L. N. Trefethen, *Rational Chebyshev approximation on the unit disk*, Numer. Math., 37 (1981), pp. 297–320.
[26] L. N. Trefethen and M. H. Gutknecht, *Padé, stable Padé, and Chebyshev-Padé approximation*, in Algorithms for Approximation, J. C. Mason and M. G. Cox, eds., Oxford University Press, New York, 1987, pp. 227–264.